High Spatiotemporal Resolution River Networks Mapping on Catchment Scale Using Satellite Remote Sensing Imagery and DEM Data

Peng Li[1, 2], Yun Zhang[1, 2], Cunren Liang[3], Houjie Wang[1, 2], and Zhenhong Li[4]

[1]Institute of Estuarine and Coastal Zone, College of Marine Geosciences, Key Lab of Submarine Geosciences and Prospecting Technology, Ministry of Education, Ocean University of China, Qingdao, China.

[2]Laboratory of Marine Geology, Qingdao National Laboratory for Marine Science and Technology, Qingdao, China.

[3]Institute of Remote Sensing and Geographic Information System, School of Earth and Space Sciences, Peking University, China.

[4]College of Geological Engineering and Geomatics, Chang'an University, Xi'an, China.

Corresponding author: Houjie Wang (hjwang@ouc.edu.cn)

Peng Li, and Yun Zhang are co-first authors of this article.

Key Points:

- We proposed a new method for mapping 10 m resolution continuous river networks on a monthly basin scale using satellite images and DEMs.

- This method provided detailed information on small- and medium-sized rivers with an overall accuracy of 95.8%.

- There is a strong positive correlation between monthly river network area and precipitation.

Abstract

Characterizing and understanding the changes in the flow regimes of rivers have been challenging. Existing global river network datasets are not updated and can only identify rivers wider than 30 m. We propose a novel automated method to map river networks on a monthly basin scale for the first time at 10-m resolution using Sentinel-1 Synthetic Aperture Radar, Sentinel-2 multispectral images, and the AW3D30 Digital Surface Model. This method achieved an overall accuracy of 95.8%. The total length of the Yellow River network produced is 40,280 km, approximately 3.2 times that of the Global River Widths from Landsat (GRWL) database, more effectively covering small and medium rivers. The monthly river geometry revealed a positive correlation between river network area and precipitation. This study is expected to provide a cost-effective alternative to accurately mapping global river networks and advance our understanding of the changes and drivers of river systems.

Plain Language Summary

Understanding the impacts of climate change and human activities on water resources across different regions greatly depends on the knowledge of river networks with high spatial and temporal resolution. Small tributaries are important components in river network evolution and water transmission. To date, several studies have mapped interannual variations in rivers with widths >30 m; however, the distribution and variations in small rivers remain unclear. By integrating multispectral and radar satellite remote sensing images as well as topographic data, we created continuous monthly river network maps at the basin scale, allowing us to capture the details of dynamic changes in river networks with higher spatiotemporal resolution. As a result, the method used in this study provides detailed information on small and medium rivers, with the length of the connected rivers being thrice that of the existing datasets. We demonstrate the possibility of mapping global river networks monthly at a resolution of 10 m, providing valuable information for global surface water resource planning and management and improving our understanding of spatial links between land and water interfaces.

1 Introduction

River networks interact with the atmosphere, vegetation, and geomorphology; play important roles in global hydrological and biogeochemical cycles; and are natural hotspots for environmental sustainability and economic growth (Raymond et al., 2013; Allen et al., 2018). Spatial characteristics, such as river surface area and river channel morphology, are essential for discharge estimation, flood forecasting, riverbed evolution, hydrogeomorphic processes, and carbon emission assessment. From a long-term and global perspective, characterizing and understanding the dynamic changes in the flow regimes of rivers have been challenging (Wu et al., 2023). Therefore, there is a pressing need to understand what contributes to global river extent changes through better observation and modeling.

However, existing river network datasets, mainly from Landsat imagery, can only identify rivers with channel widths greater than 30 m (Pekel et al., 2016; Allen & Pavelsky, 2018), and ignore the temporal variations in rivers narrower than 30 m (Lu et al., 2020). Small river ecosystems are surprisingly active, with frequent land-atmosphere interactions and 50% of the total carbon emissions (Raymond et al., 2013; Butman et al., 2016). Ignoring the importance of small rivers underestimates the role of river networks in biogeochemical cycles (Lu et al., 2021).

64 Thus, large-scale, accurate, and up-to-date river network maps are beneficial for sustainable
65 development, government decision-making, and public awareness.

66   Currently available global and regional river network datasets are mainly derived from
67 digital elevation models (DEMs) or remote sensing images (Li et al., 2022). The key to developing
68 hydrological maps from DEMs is to calculate the flow direction of each pixel (Strong & Mudd,
69 2022; Tarolli & Mudd, 2020), such as the HydroSHEDS and MERIT Hydro datasets.
70 HydroSHEDS is a global hydrological dataset obtained from the SRTM elevation data with a
71 resolution of 90 m (Lehner & Grill, 2013). Yamazaki et al. (2019) generated the MERIT Hydro
72 dataset, which effectively solved the problem of limited coverage of HydroSHEDS at high
73 latitudes. However, vertical uncertainties in the DEM data may distort the topographic slope and
74 further affect the flow direction estimation. In addition, global DEM data sources are not updated
75 in a timely manner, making it difficult to reflect the dynamic changes in river networks (Rinne et
76 al. 2011; Schenk et al. 2014).

77   In recent years, Earth observation satellites have become an effective method for obtaining
78 long-term time series, accurate distributions, and dynamic changes in global river networks (Gong
79 et al., 2013; Yamazaki et al., 2015; Feng et al., 2019). Using Google Earth Engine (GEE) cloud-
80 based computing resources, the storage, computing, and analysis capabilities of remote sensing
81 big data have greatly improved (Gorelick et al., 2017). Pekel et al. (2016) produced a Global
82 Surface Water (GSW) dataset at 30 m resolution using GEE and Landsat images, which presents
83 the probability of surface water inundation for every pixel recorded by Landsat over the past four
84 decades. Allen & Pavelsky (2018) built the Global River Widths from Landsat (GRWL) Database
85 and estimated the total surface area of rivers and streams ⩾30 m wide at mean annual discharge,
86 which is approximately 44% higher than previous estimates based on extrapolations of small
87 sample sizes (Raymond et al., 2013). Compared with Landsat images, commercial optical remote
88 sensing images usually have higher spatial resolution and richer spectral information; however,
89 they are also affected by clouds and shadows when identifying water bodies.

90   Synthetic aperture radar (SAR) sensors operating in the microwave region of the
91 electromagnetic spectrum are not limited by meteorological conditions and can penetrate clouds
92 and vegetation cover. The fusion of SAR and optical images for water classification has been
93 proven to capture the extent of surface water bodies at a higher spatial and temporal resolution
94 without being affected by clouds (Slinski et al., 2019; Li et al., 2023). However, river networks
95 extracted from remote-sensing images are fragmented and exhibit poor connectivity. Recent
96 studies have suggested that a combination of satellite remote sensing imagery and DEM data can
97 accurately extract continuous river networks and monitor their dynamic changes (Jones, 2019).
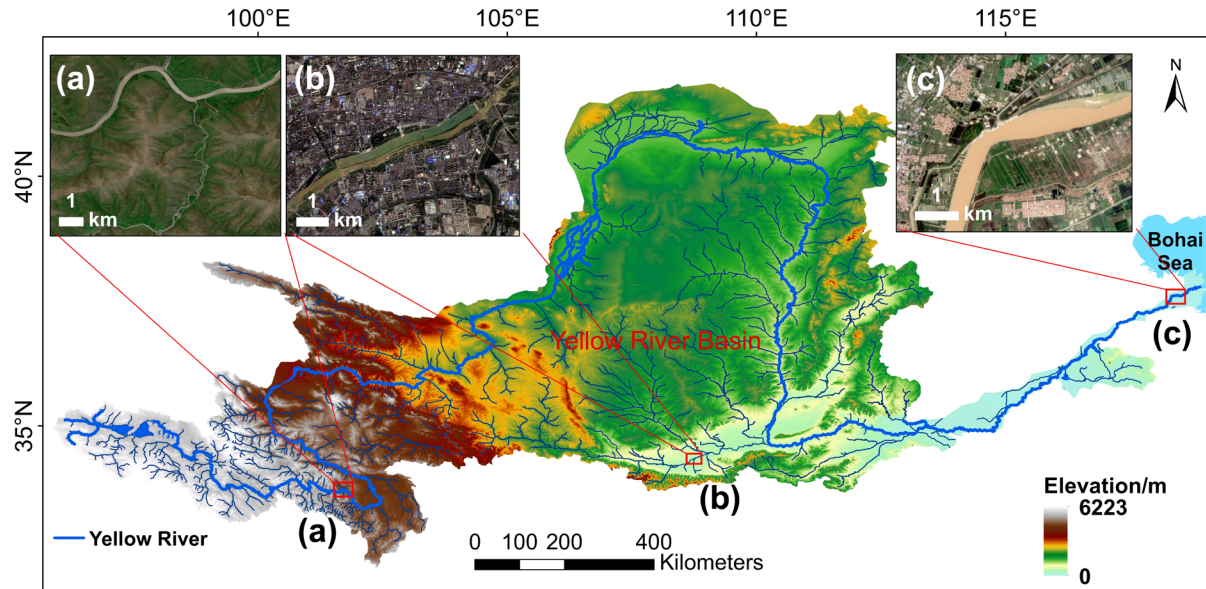
98   To address these challenges, we developed a new automated method that integrates Sentinel-
99 1 SAR, Sentinel-2 multispectral images, and DEM data to generate monthly river network maps
100 of the Yellow River basin (YRB) at a resolution of 10 m. The constraint of the topography on the
101 river flow direction was used to solve the problem of poor connectivity. Furthermore, we evaluate
102 the accuracy of the method and compare it with existing datasets. Finally, we investigated the
103 correlation between river network areas and climatic factors.

2 Materials and Methods

2.1 Study Area

The Yellow River is the second largest river in China, originating in the Qinghai-Tibetan Plateau and flowing eastward through the Loess Plateau and North China Plain to the Bohai Sea (Wu et al., 2017; Syvitski et al., 2022). The main stream of the Yellow River has a total length of more than 5,400 km and a drainage area of more than 750,000 km^2 (Wang et al., 2007). The upper reaches of the Yellow River are dominated by mountains, whereas the middle and lower reaches are dominated by plains and hills (Figure 1a–c), forming the youngest delta in China (Wang et al., 2022). Nearly 90% of the sediment originates from the middle reaches, and 60% of the river runoff originates from the upper reaches (Wang et al., 2017; Zhu et al., 2021; Chang et al., 2022).
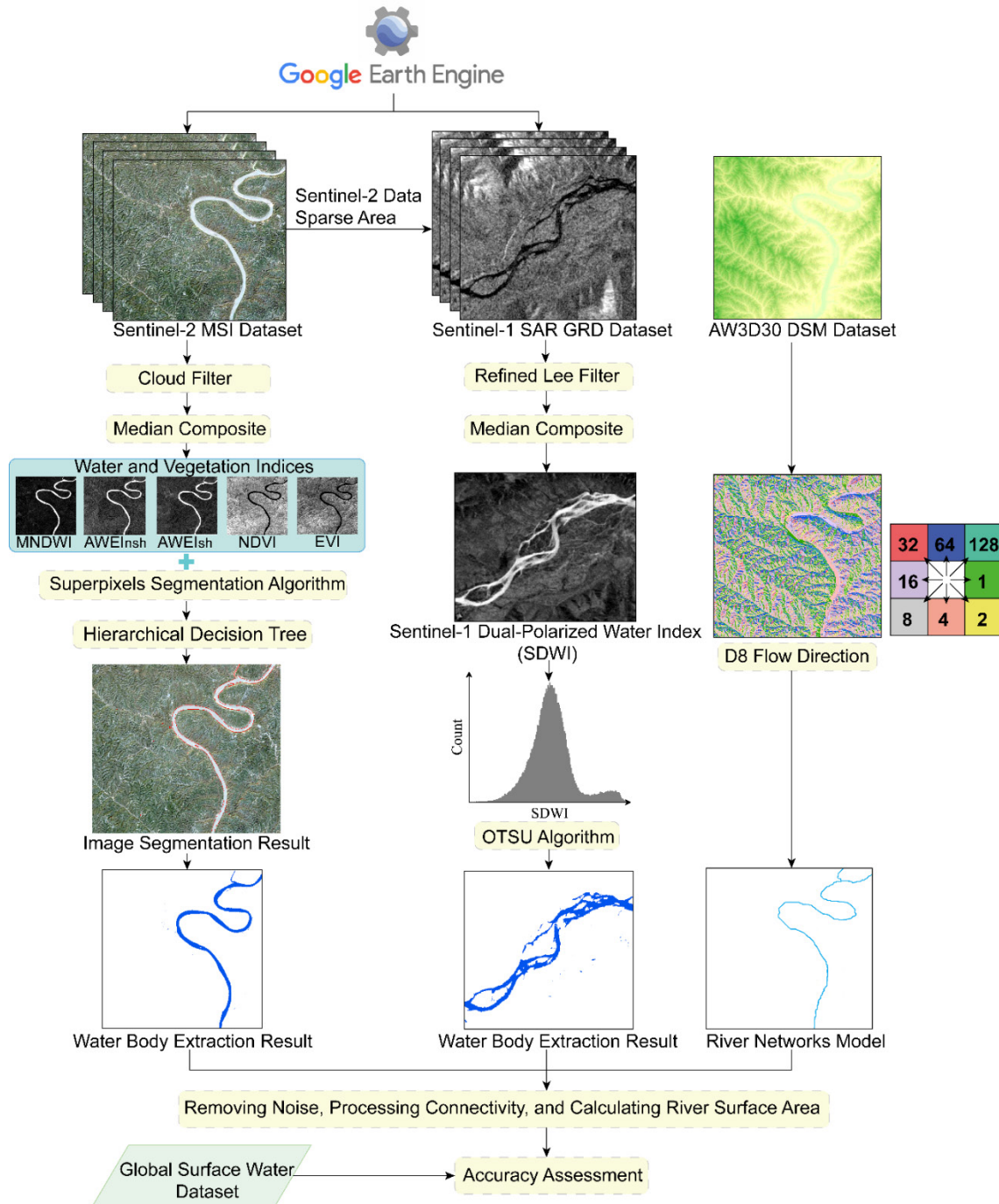
The Yellow River provides water to 15% of China's arable land and 12% of the population, accounting for 2.2% of the national runoff (Yin et al., 2021). It is characterized by water shortages, less water and more sediment, and different sources of water and sediment (Wang et al., 2019). With the gradual implementation of soil and water conservation and ecological restoration projects, the intensity of soil erosion in the Loess Plateau has decreased significantly, and the sediment load in the main stream of the Yellow River has shown a significant downward trend over the past 20 years (Syvitski et al., 2022). However, with the increasing frequency and intensity of extreme weather events, particularly rainstorms and droughts, changes in hydrological processes in the YRB are aggravating, posing challenges to water resource management, flood prevention, and water and sediment regulation (Lv et al., 2018; Shao et al., 2021). Unfortunately, the existing river network datasets derived from Landsat remote sensing images or DEMs limit the dynamic monitoring of temporal and spatial changes of small and medium-sized rivers in the basin.

Figure 1. Location of the study area. (a) Upper reaches, (b) middle reaches, and (c) lower reaches in the Yellow River Basin were derived from Sentinel-2 RGB imagery. Note that, RGB bands include band 4 (red), band 3 (green), and band 2 (blue).

130   2.2 Methods

131   The process of river network generation mainly includes the following two parts: (1) water
132   body extraction by median composite generation and threshold segmentation algorithms based on
133   filtered Sentinel-2 multispectral and Sentinel-1 SAR images, and (2) river network extraction
134   based on Advanced Land Observing Satellite (ALOS) World 3D-30 m (AW3D30) Digital Surface
135   Model (DSM) flow modeling, noise removal, and connectivity processing. Figure 2 shows the
136   workflow of the proposed method.

137

138   **Figure 2**. Workflow of river networks extraction in the Yellow River Basin.

139   2.2.1 Datasets

140   Sentinel-2 multispectral remote sensing images were used as the main data source (Drusch
141 et al., 2012), and Sentinel-1 SAR images were used to fill observation gaps caused by cloud cover
142 and missing data. The Sentinel-2 Level-2A products provide orthorectified atmospherically
143 corrected surface reflectance and can be freely obtained on the GEE platform. A total of 6,357
144 Sentinel-2 images were selected between January 2019 and December 2019. Considering the
145 shortage of Sentinel-2 images with cloud cover of less than 20% in cloudy areas and data-missing
146 regions (Yang et al., 2020b), Sentinel-1 Level-1 Ground Range Detected (GRD) products were
147 selected as supplements, which consist of focused SAR magnitude data (Torres et al., 2012).

148   The AW3D30 DSM was obtained by resampling the AW3D product with a spatial
149 resolution of 30 m and a vertical accuracy of 5 m (Tadono et al., 2014). Among the publicly
150 available global digital elevation model (DEM) datasets, AW3D30 has the highest accuracy in
151 mountainous areas (Liu et al., 2019; P. Li et al., 2021). Therefore, we used AW3D30 as auxiliary
152 data to represent the topographic relief and constrain the river flow direction in the YRB.

153   Other datasets included the GSW dataset, 2020 Global Land Cover Map released by
154 Environmental Systems Research Institute (known as ESRI), and the fifth-generation European
155 Centre for Medium-Range Weather Forecasts (ECMWF) reanalysis (ERA5) dataset. The GSW
156 dataset is used to verify the accuracy of the results. ESRI 2020 Land Cover data were used to
157 generate scatter density maps of water and non-water samples and determine the threshold for
158 water body extraction. These data can be accessed from the GEE's public data catalog.
159 Temperature, precipitation, and evaporation were derived from ERA5 to evaluate the impact of
160 climate change on river surface area.

161   2.2.2 Water Body Extraction

162   For the Sentinel-2 multispectral images, in order to effectively reduce the impact of
163 omission errors from clouds and cloud shadow detection, opaque clouds and cirrus clouds were
164 removed using the QA60 band on GEE. The position of the cloud shadow was determined based
165 on the solar geometric angle and elevation angle attributes of each image, and dark pixels generated
166 by the cloud shadow were masked. These filtered images were clipped to the study area to derive
167 a median composite with a cloud cover limit of less than 20%.

168   The median image composite method was computationally efficient and robust. Sentinel-
169 2 images processed by cloud filtering every month were collected, and the median of each pixel
170 value was calculated to generate a composite image every month. This method was also applied
171 to Sentinel-1 images after filtering. Compared to a single Sentinel-1 image, the median composite
172 image can suppress speckle noise (Figure S1).

173   We used Simple Non-Iterative Clustering (SNIC) superpixels segmentation algorithm
174 combining decision trees to segment water bodies (Wang et al., 2023) (Figure S2 and S6). Using
175 superpixels as subsequent processing units can greatly accelerate data processing efficiency and
176 reduce the complexity of identifying water bodies.

177   We then combined the automatic water extraction index (AWEI) (Feyisa et al., 2014),
178 modified normalized difference water index (MNDWI) (Xu, 2006), normalized difference
179 vegetation index (NDVI) (Rouse et al., 1974), and enhanced vegetation index (EVI) (Huete et al.,
180 2002) to distinguish between water bodies and non-water areas in Sentinel-2 images (Zou et al.,
181 2018; Deng et al., 2019). The AWEI is divided into $AWEI_{nsh}$ and $AWEI_{sh}$ based on the difference

in noise sources produced by different types of areas. $AWEI_{nsh}$ can effectively eliminate non-water pixels on dark building surfaces in urban background areas, that is for situations where shadows are not the main noise. $AWEI_{sh}$ works mainly for situations in which shadows are the main problem. These indices are defined as follows:

$$AWEI_{nsh} = 4 \times (\rho_{Green} - \rho_{SWIR1}) - (0.25 \times \rho_{NIR} + 2.75 \times \rho_{SWIR2}) \qquad (1)$$

$$AWEI_{sh} = \rho_{Blue} + 2.5 \times \rho_{Green} - 1.5 \times (\rho_{NIR} + \rho_{SWIR1}) - 0.25 \times \rho_{SWIR2} \qquad (2)$$

$$MNDWI = \frac{\rho_{Green} - \rho_{SWIR1}}{\rho_{Green} + \rho_{SWIR1}} \qquad (3)$$

$$EVI = 2.5 \times \frac{(\rho_{NIR} - \rho_{Red})}{(1 + \rho_{NIR} + 6 \times \rho_{Red} - 7.5 \times \rho_{Blue})} \qquad (4)$$

$$NDVI = \frac{\rho_{NIR} - \rho_{Red}}{\rho_{NIR} + \rho_{Red}} \qquad (5)$$

where ρ_{Blue}, ρ_{Green}, ρ_{Red}, ρ_{NIR}, ρ_{SWIR1}, and ρ_{SWIR2} are the surface reflectance values of the Sentinel-2 Blue (band 2), green (band 3), red (band 4), NIR (band 8), SWIR1 (band 11), and SWIR2 (band 12) bands, respectively. These bands were resampled to 10 m.

We trained the decision tree classifier by collecting 10,093 water samples and 9,905 non-water samples (see Text S1), and generated scatter density maps for water and non-water bodies (Figure S4). Of the non-water sample points, 99.81% had MNDWI-EVI<0, whereas 92.39% of the water sample points had MNDWI-EVI>0 (Figure S4e). Of the non-water sample points, 99.83% had MNDWI-NDVI<0, whereas 91.43% of the water sample points had MNDWI-NDVI>0 (Figure S4f). Furthermore, 95.31% of the water sample points show $AWEI_{nsh}$>-0.6 (Figure S4g), whereas 91.21% of the water sample points show $AWEI_{sh}$>0 (Figure S4h). Therefore, we proposed a new threshold segmentation algorithm for Sentinel-2 water body detection, that is, only the pixels meeting the criteria (($AWEI_{nsh}$>-0.6 or $AWEI_{sh}$>0) and (MNDWI>EVI or MNDWI>NDVI)) were classified as open surface water pixels, and the remaining were classified as non-water pixels. Paddy fields with spectral and water color characteristics similar to those of rivers can easily cause confusion and reduce the accuracy of river network extraction. The NDVI time-series features of the water objects were analyzed to eliminate paddy fields from the results (Figure S5).

We marked pixels in the missing areas of the Sentinel-2 images as no data and replaced them with SAR water extraction results after completing the Sentinel-2 water extraction. For Sentinel-1 SAR images, we used a refined Lee filter to suppress speckle noise while preserving the image details (Lee et al., 1999; Amitrano et al., 2018). This filter uses a non-square edge direction window to maintain the edge information, and all elements of the covariance matrix are filtered using the same parameters to prevent crosstalk between the channels. By calculating Sentinel-1 Dual-Polarized Water Index (SDWI) (Jia et al., 2019), the difference between water and non-water bodies are amplified, making the histogram of water bodies resemble a bimodal distribution. Then, the water threshold in block processing was obtained using the maximum inter-class difference threshold segmentation (OTSU) algorithm to segment and binarize the Sentinel-1 median composite images (Otsu, 1979).

218   2.2.3 Delineation of River Centerlines

219   The river centerline was extracted using the RivWidthCloud algorithm proposed by Yang
220 et al. (2020a), which can be directly invoked on the GEE platform. The algorithm was based on
221 the results of the binary water body, which were divided into three steps: (1) calculation of the
222 distance between each river pixel and the nearest non-river pixel, (2) convolution of the distance
223 map to obtain the gradient map, and (3) skeletonization and refinement iterations (Figure S7).

224   Owing to the interference of non-water features, such as mountain shadows, snow, and ice,
225 there are errors in the water body extraction results. We used the AW3D30 DSM data to fill in the
226 depressions, calculate the D8 flow direction (Greenlee, 1987), estimate confluence accumulations,
227 construct river network models, and generate buffers. This method can effectively reduce the errors
228 caused by mountain shadows and maximally preserve the integrity of water information.

229   The flow model constructed using the AW3D30 DSM considers the adjacency relationship
230 between river pixels and can generate continuous river networks. Therefore, we fused it with river
231 network results extracted from remote sensing images, made directional connections to the
232 fractured river networks, and generated an accurate and continuous river network with a spatial
233 resolution of 10 m. Next, we compared the extracted results with those extracted from existing
234 river network datasets and existing algorithms and quantitatively evaluated the accuracy of the
235 results in terms of river length, river system density, and river network surface area.
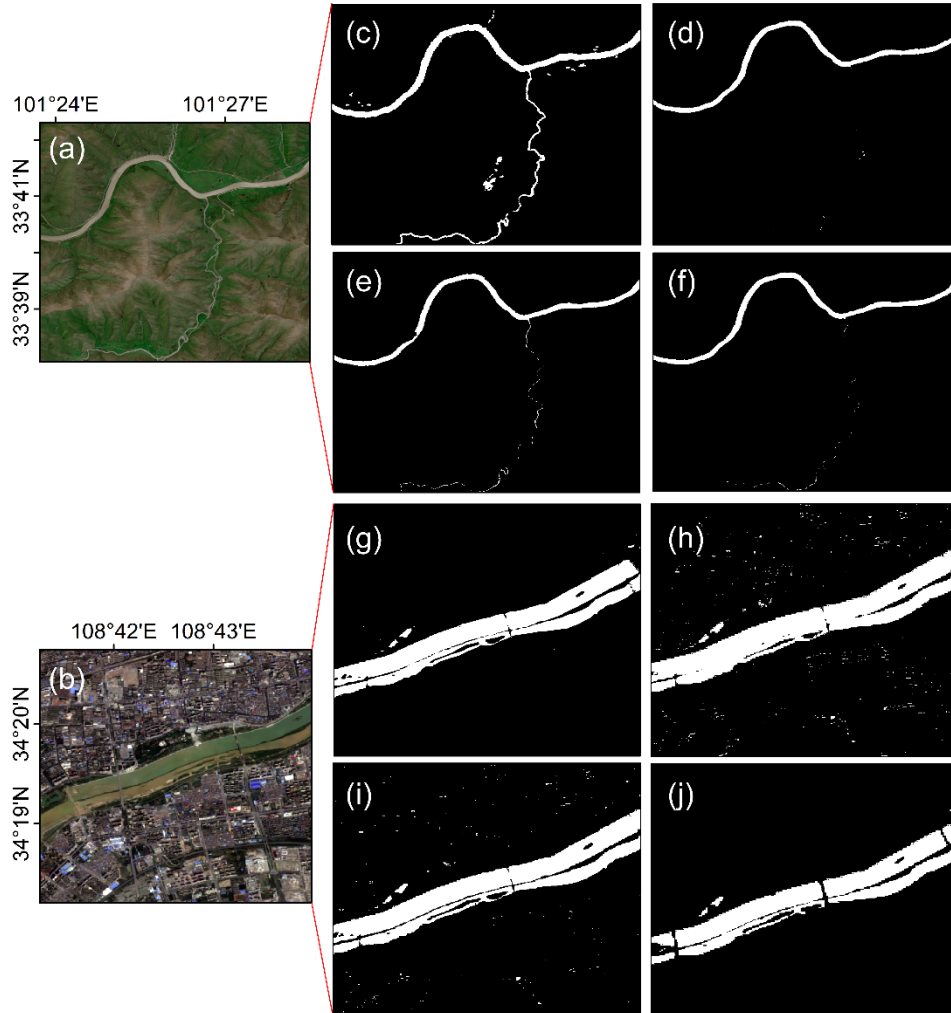
3 Results

236 **3 Results**

237   Figure S10 shows the dynamic changes in monthly river networks in the YRB in 2019.
238 River density, that is, the ratio of river length to catchment area, increased from 0.038 km^{-1} in
239 January and February to 0.042 km^{-1} in March and April, owing to upstream melting. The rivers
240 developed rapidly in May and entered the wet season in July, which significantly improved the
241 connectivity of river networks. At this time, the total length of the river was 40280 km and the
242 density of the river system was 0.053 km^{-1}, both of which increased to the annual maximum. After
243 entering September, the rainy season turned to normal, and the density of the river system
244 gradually decreased.

245   To validate the reliability of our algorithm, we used 2,556 random "true water" sampling
246 points and 2,430 random "true non-water" points (Text S2 and Figure S8). The results indicated
247 that the overall accuracy was as high as 95.77%. Furthermore, the user accuracy of 95.83% was
248 obtained by dividing the accurately classified pixels by the total numbers of pixels classified in
249 water, corresponding to complement of the commission error. In addition, the producer accuracy
250 also reached a high level of 95.84%, which is the number of reference sites classified accurately
251 divided by the total number of reference sites for water, representing complement of the omission
252 error (Figure 4g and Table S1).

253   Furthermore, we compared our method (Figure 3c, 3g) with other algorithms for detecting
254 river networks using Sentinel-2 imagery, including MNDWI (Figure 3d, 3h), an approach based
255 on spectral indices and pixels (Zou et al., 2018) (Figure 3e, 3i), and the active-passive surface
256 water classification (APWC) method proposed by Slinski et al. (2019) (Figure 3f and 3j). As there
257 are many medium and large cities with dense populations in the mainstem of the YRB, some pixels
258 in the area are always covered by shadows because high-rise buildings are too high or the building
259 spacing is too small. The proposed algorithm effectively suppressed this type of shadow noise.
260 Note that our algorithm does not require manual editing or data annotation, which makes it possible

261 to realize the automatic mapping of large-scale river networks with high spatial resolution on a
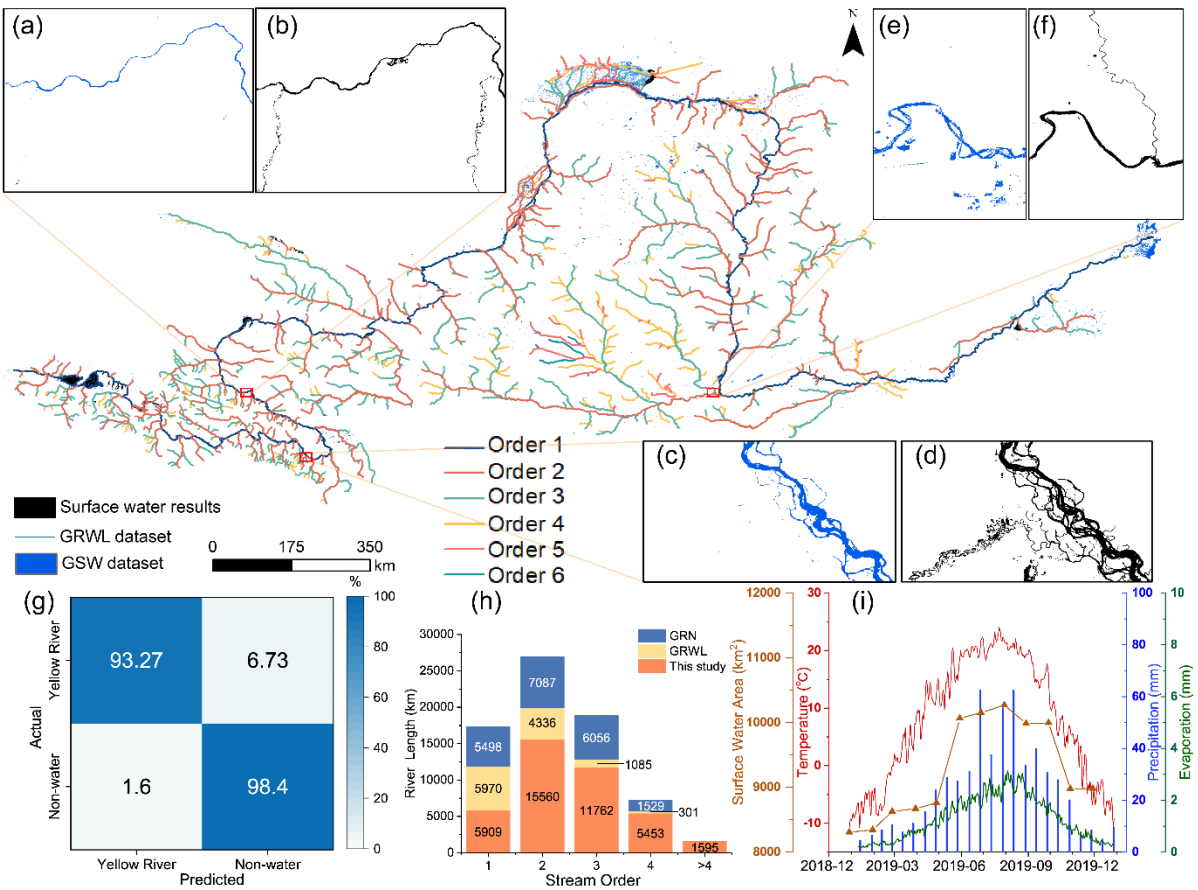262 high-performance computing platform.

263

Figure 3. Comparisons of the results of this method with other methods. Typical city (a) and
mountain area (b) correspond to Figure 1a and 1b; (c) and (g) show the results of our method; (d)
and (h) present the results of MNDWI; (e) and (i) are the results of Zou et al. (2018); (f) and (j)
are the results of the APWC method proposed by Slinski et al. (2019).

4 Discussion

269 The results were superimposed on the GRWL and GSW datasets to qualitatively evaluate
270 the spatial distribution and details of the river networks (Figure 4). The results show that our
271 method can more effectively enhance the contrast between the fine river and the surrounding
272 background, and can extract more small rivers (Figure 4a-f). However, river networks were the
273 most accurate and complete when the river width was greater than 30 m, whereas broken river
274 lines may exist in areas less than 30 m wide. In addition, the influence of ice and snow cover on
275 river extraction errors cannot be completely eliminated in the Qinghai-Tibet Plateau.

276 We further calculated the drainage density and open water fraction (OWF, i.e., the ratio of
277 the water surface area to the catchment area) and quantified the accuracy of our extraction results

278 using existing river network datasets. The drainage density of Yellow River networks map we
279 determined is approximately three times higher than that of the existing GRWL and GSW datasets.
280 The OWF index of the Yellow River network map was approximately 3.2 times that of the GRWL
281 dataset. The GSW dataset contained artificial wetlands that were not considered part of the river
282 networks in this study. Therefore, the OWF index of the GSW dataset is higher than that of our
283 results. The superior performance of our method can be attributed to the following reasons: first,
284 we used Sentinel-2 imagery with high spatial resolution to extract more small streams than Landsat
285 images. Second, the use of Sentienl-1 to compensate for areas of Sentinel-2 images with clouds
286 and missing data can improve temporal resolution and capture monthly changes in the YRB
287 (Figure S9).

Figure 4. Comparisons with different river datasets and our results. The base map shows Yellow River networks results and the existing the Global River Widths from the Landsat (GRWL) database. (a), (c), and (e) Water surface results of the existing Global Surface Water (GSW) dataset. (b), (d), and (f) Water surface results of our method. (g) Confusion matrix for the automated accuracy assessment of our method. (h) Comparison of the river length (km) in the results of this study, GRWL dataset and Global River Networks (GRN) dataset. (i) The relationship between the surface area (yellow line), precipitation (blue column), temperature (red line), and evaporation (green line) in the Yellow River Basin.

297 The rules established by Yan et al. (2019) were used to define and code river networks that
298 could describe the topological relationships, hierarchical structures, and hydraulic connections of
299 rivers at the same or different orders. The river lengths in our dataset were compared to those in

the GRWL and Global River Network (GRN) datasets (Yan et al., 2019) in Figure 4h. Overall, the total length (40,280 km) of the connected rivers provided in our results was 28,587 km longer than all rivers in the GRWL dataset, and 19,389 km longer than all rivers in the GRN dataset. Particularly, the length of connected rivers of order ≥4 in our dataset is longer than that of the GRWL dataset and GRN dataset, indicating that our results have a better coverage of small and medium-sized rivers (Figure S11).

At the catchment scale, the scale dependence of runoff was attributed to spatial differences in precipitation, lithology, channel width, and catchment morphology. Assuming that the changes in soil water content and infiltration are negligible, the change in river network area depends mainly on the difference between precipitation and evaporation. Figure 4i indicates that the change in the water surface area during the rainy season was significantly greater than that during the dry season. The minimum area of the river networks appeared in January, with a total area of 8,306 km^2 and the maximum area occurred in August, with a total area of 10,267 km^2. Precipitation and evaporation in the YRB were positively correlated with monthly changes in river network area. Considering that the average monthly precipitation is 10-20 times that of evaporation, the river network area is primarily controlled by seasonal precipitation changes, increasing after the spring and summer rainy seasons and decreasing in autumn and winter.

5 Conclusions

Studies on the impacts of climate change and human activity on river basins are highly dependent on the spatial and temporal distributions of river networks. However, the lack of accurate river networks with high spatiotemporal resolution in many regions makes these impacts poorly understood. In this study, we proposed a method for generating catchment-scale continuous river network maps for every month by integrating Sentinel-1 SAR and Sentinel-2 multispectral images with AW3D30 DSM data. This method can reveal detailed information on small and medium-sized rivers, with the length of the connected rivers being three times that of the existing datasets. The proposed detection rule can be used to extract large river network areas rapidly. The error caused by water spectral and morphological diversity as well as seasonal changes is reduced to the greatest extent, which makes large-scale and long-term water extraction more universal.

Compared to existing water extraction algorithms, the proposed method demonstrates its capability and effectiveness in the shadow noise environment of urban high-rise buildings and mountainous areas, indicating that it has certain advantages over other single water indices. In addition, compared to existing river network products, this method improves the extraction area of water and the extraction rate of small rivers. Therefore, it provides an alternative economic means for the long-term monitoring of river network changes, quantifying, and understanding the contribution of human activities and climate change to river channel evolution. In the future, further integration of the Surface Water and Ocean Topography mission will facilitate the rapid acquisition of river width, elevation, and discharge parameters on a global scale.

Open Research

Acknowledgements

References

Allen, G. H., & Pavelsky, T. M. (2018). Global extent of rivers and streams. *Science*, *361*(6402), 585–588. https://doi.org/10.1126/science.aat0636

Allen, G. H., Pavelsky, T. M., Barefoot, E. A., Lamb, M. P., Butman, D., Tashie, A., & Gleason, C. J. (2018). Similarity of stream width distributions across headwater systems. *Nature Communications*, *9*(1), 610. https://doi.org/10.1038/s41467-018-02991-w

Amitrano, D., Di Martino, G., Iodice, A., Riccio, D., & Ruello, G. (2018). Unsupervised Rapid Flood Mapping Using Sentinel-1 GRD SAR Images. *IEEE Transactions on Geoscience and Remote Sensing*, *56*(6), 3290–3299. https://doi.org/10.1109/TGRS.2018.2797536

Butman, D., Stackpoole, S., Stets, E., McDonald, C. P., Clow, D. W., & Striegl, R. G. (2016). Aquatic carbon cycling in the conterminous United States and implications for terrestrial carbon accounting. *Proceedings of the National Academy of Sciences*, *113*(1), 58–63. https://doi.org/10.1073/pnas.1512651112

Chang, M., Li, P., Sun, Y., Wang, H., & Li, Z. (2022). Mapping Dynamic Turbidity Maximum Zone of the Yellow River Estuary from 38 Years of Landsat Imagery. *Remote Sensing*, *14*(15), 3782. https://doi.org/10.3390/rs14153782

Deng, Y., Jiang, W., Tang, Z., Ling, Z., & Wu, Z. (2019). Long-Term Changes of Open-Surface Water Bodies in the Yangtze River Basin Based on the Google Earth Engine Cloud Platform. *Remote Sensing*, *11*(19), 2213. https://doi.org/10.3390/rs11192213

Drusch, M., Del Bello, U., Carlier, S., Colin, O., Fernandez, V., Gascon, F., et al. (2012). Sentinel-2: ESA's Optical High-Resolution Mission for GMES Operational Services. *Remote Sensing of Environment*, *120*, 25–36. https://doi.org/10.1016/j.rse.2011.11.026

Feng, S., Liu, S., Huang, Z., Jing, L., Zhao, M., Peng, X., et al. (2019). Inland water bodies in China: Features discovered in the long-term satellite data. *Proceedings of the National Academy of Sciences*, *116*(51), 25491–25496. https://doi.org/10.1073/pnas.1910872116

Feyisa, G. L., Meilby, H., Fensholt, R., & Proud, S. R. (2014). Automated Water Extraction Index: A new technique for surface water mapping using Landsat imagery. *Remote Sensing of Environment*, *140*, 23–35. https://doi.org/10.1016/j.rse.2013.08.029

Gong, P., Wang, J., Yu, L., Zhao, Y., Zhao, Y., Liang, L., et al. (2013). Finer resolution observation and monitoring of global land cover: first mapping results with Landsat TM and ETM+ data. *International Journal of Remote Sensing*, *34*(7), 2607–2654. https://doi.org/10.1080/01431161.2012.748992

Gorelick, N., Hancher, M., Dixon, M., Ilyushchenko, S., Thau, D., & Moore, R. (2017). Google Earth Engine: Planetary-scale geospatial analysis for everyone. *Remote Sensing of Environment*, *202*, 18–27. https://doi.org/10.1016/j.rse.2017.06.031

Greenlee, D. D. (1987). Raster and vector processing for scanned linework. *Photogrammetric Engineering and Remote Sensing*, *53*(10), 1383–1387.

Huete, A., Didan, K., Miura, T., Rodriguez, E. P., Gao, X., & Ferreira, L. G. (2002). Overview of the radiometric and biophysical performance of the MODIS vegetation indices. *Remote Sensing of Environment*, *83*(1), 195–213. https://doi.org/10.1016/S0034-4257(02)00096-2

Jia, S., Xue, D., Li, C., Zheng, J., & Li, W. (2019). Study on new method for water area information extraction based on Sentinel-1 data. *Yangtze River*, *50*(2), 213–217. https://doi.org/10.16232/j.cnki.1001-4179.2019.02.038.

Jones, J. W. (2019). Improved Automated Detection of Subpixel-Scale Inundation—Revised Dynamic Surface Water Extent (DSWE) Partial Surface Water Tests. *Remote Sensing*, *11*(4), 374. https://doi.org/10.3390/rs11040374

Lee, J.-S., Grunes, M. R., & de Grandi, G. (1999). Polarimetric SAR speckle filtering and its implication for classification. *IEEE Transactions on Geoscience and Remote Sensing*, *37*(5), 2363–2373. https://doi.org/10.1109/36.789635

Lehner, B., & Grill, G. (2013). Global river hydrography and network routing: baseline data and new approaches to study the world's large river systems. *Hydrological Processes*, *27*(15), 2171–2186. https://doi.org/10.1002/hyp.9740

Li, D., Xue, Y., Qin, C., Wu, B., Chen, B., & Wang, G. (2022). A bankfull geometry dataset for major exorheic rivers on the Qinghai-Tibet Plateau. *Scientific Data*, *9*(1). https://doi.org/10.1038/s41597-022-01614-w

Li, J., Li, L., Song, Y., Chen, J., Wang, Z., Bao, Y., et al. (2023). A robust large-scale surface water mapping framework with high spatiotemporal resolution based on the fusion of multi-source remote sensing data. *International Journal of Applied Earth Observation and Geoinformation*, *118*, 103288. https://doi.org/10.1016/j.jag.2023.103288

Li, P., Li, Z., Dai, K., Al-Husseinawi, Y., Feng, W., & Wang, H. (2021). Reconstruction and Evaluation of DEMs From Bistatic Tandem-X SAR in Mountainous and Coastal Areas of China. *IEEE Journal of Selected Topics in Applied Earth Observations and Remote Sensing*, *14*, 5152–5170. https://doi.org/10.1109/JSTARS.2021.3073782

Li, P., Zhang, Y., Liang, C., Wang, H., & Li, Z. (2023). High-Resolution Satellite-Derived River Network of the Yellow River Basin. [Software]. Zenodo. https://doi.org/10.5281/zenodo.10205284

Liu, K., Song, C., Ke, L., Jiang, L., Pan, Y., & Ma, R. (2019). Global open-access DEM performances in Earth's most rugged region High Mountain Asia: A multi-level assessment. *Geomorphology*, *338*, 16–26. https://doi.org/10.1016/j.geomorph.2019.04.012

Lu, X., Yang, K., Lu, Y., Gleason, C. J., Smith, L. C., & Li, M. (2020). Small Arctic rivers mapped from Sentinel-2 satellite imagery and ArcticDEM. *Journal of Hydrology*, *584*, 124689. https://doi.org/10.1016/j.jhydrol.2020.124689

Lu, X., Yang, K., Bennett, M. M., Liu, C., Mao, W., Li, Y., et al. (2021). High-resolution satellite-derived river network map reveals small Arctic river hydrography. *Environmental Research Letters*, *16*(5), 054015. https://doi.org/10.1088/1748-9326/abf463

Lv, M., Ma, Z., & Lv, M. (2018). Effects of Climate/Land Surface Changes on Streamflow With Consideration of Precipitation Intensity and Catchment Characteristics in the Yellow River Basin. *Journal of Geophysical Research: Atmospheres*, *123*(4), 1942–1958. https://doi.org/10.1002/2017JD027625

Muñoz Sabater, J. (2019): ERA5-Land hourly data from 1950 to present. [Dataset]. Copernicus Climate Change Service (C3S) Climate Data Store (CDS), https://doi.org/10.24381/cds.e2161bac

Otsu, N. (1979). A Threshold Selection Method from Gray-Level Histograms. *IEEE Transactions on Systems, Man, and Cybernetics*, *9*(1), 62–66. https://doi.org/10.1109/TSMC.1979.4310076

Pekel, J.-F., Cottam, A., Gorelick, N., & Belward, A. S. (2016). High-resolution mapping of global surface water and its long-term changes. *Nature*, *540*(7633), 418–422. https://doi.org/10.1038/nature20584

Raymond, P. A., Hartmann, J., Lauerwald, R., Sobek, S., McDonald, C., Hoover, M., et al. (2013). Global carbon dioxide emissions from inland waters. *Nature*, *503*(7476), 355–359. https://doi.org/10.1038/nature12760

Rouse, J. W., Haas, R. H., Schell, J. A., & Deering, D. W. (1974). Monitoring vegetation systems in the Great Plains with ERTS. *NASA Spec. Publ*, *351*(1), 309.

Shao, R., Zhang, B., He, X., Su, T., Li, Y., Biao, L., et al. (2021). Historical Water Storage Changes Over China's Loess Plateau. *Water Resources Research*, *57*. https://doi.org/10.1029/2020WR028661

Slinski, K. M., Hogue, T. S., & McCray, J. E. (2019). Active-Passive Surface Water Classification: A New Method for High-Resolution Monitoring of Surface Water Dynamics. *Geophysical Research Letters*, *46*(9), 4694–4704. https://doi.org/10.1029/2019gl082562

Strong, C. M., & Mudd, S. M. (2022). Explaining the climate sensitivity of junction geometry in global river networks. *Proceedings of the National Academy of Sciences*, *119*(50), e2211942119. https://doi.org/10.1073/pnas.2211942119

Syvitski, J., Restrepo, J., Saito, Y., Overeem, I., Vörösmarty, C., Wang, H., & Olago, D. (2022). Earth's sediment cycle during the Anthropocene. *Nature Reviews Earth & Environment*, *3*, 1–18. https://doi.org/10.1038/s43017-021-00253-w

Tadono, T., Ishida, H., Oda, F., Naito, S., Minakawa, K., & Iwamoto, H. (2014). Precise Global DEM Generation by ALOS PRISM. *ISPRS Annals of the Photogrammetry, Remote Sensing and Spatial Information Sciences*, *II–4*, 71–76. https://doi.org/10.5194/isprsannals-II-4-71-2014

Tarolli, P., & Mudd, S. M. (2020). *Remote Sensing of Geomorphology* (Vol. 23). Elsevier.

Torres, R., Snoeij, P., Geudtner, D., Bibby, D., Davidson, M., Attema, E., et al. (2012). GMES Sentinel-1 mission. *Remote Sensing of Environment*, *120*, 9-24. https://www.sciencedirect.com/science/article/pii/S0034425712000600

Wang, G., Li, P., Li, Z., Liang, C., & Wang, H. (2022). Coastal subsidence detection and characterization caused by brine mining over the Yellow River Delta using time series InSAR and PCA. *International Journal of Applied Earth Observation and Geoinformation*, *114*, 103077. https://doi.org/10.1016/j.jag.2022.103077

Wang, H., Yang, Z., Saito, Y., Liu, J. P., Sun, X., & Wang, Y. (2007). Stepwise decreases of the Huanghe (Yellow River) sediment load (1950–2005): Impacts of climate change and human activities. *Global and Planetary Change*, *57*(3), 331–354. https://doi.org/10.1016/j.gloplacha.2007.01.003

Wang, H., Wu, X., Bi, N., Li, S., Yuan, P., Wang, A., et al. (2017). Impacts of the dam-orientated water-sediment regulation scheme on the lower reaches and delta of the Yellow River (Huanghe): A review. *Global and Planetary Change*, *157*, 93–113. https://doi.org/10.1016/j.gloplacha.2017.08.005

Wang, M., Mao, D., Xiao, X., Song, K., Jia, M., Ren, C., & Wang, Z. (2023). Interannual changes of coastal aquaculture ponds in China at 10-m spatial resolution during 2016–2021. *Remote Sensing of Environment*, *284*, 113347. https://doi.org/10.1016/j.rse.2022.113347

Wang, Y., Zhao, W., Wang, S., Feng, X., & Liu, Y. (2019). Yellow River water rebalanced by human regulation. *Scientific Reports*, *9*(1), 9707. https://doi.org/10.1038/s41598-019-46063-5

Wu, Q., Ke, L., Wang, J., Pavelsky, T. M., Allen, G. H., Sheng, Y., et al. (2023). Satellites reveal hotspots of global river extent change. *Nature Communications*, *14*(1), 1587. https://doi.org/10.1038/s41467-023-37061-3

Wu, X., Bi, N., Xu, J., Nittrouer, J. A., Yang, Z., Saito, Y., & Wang, H. (2017). Stepwise morphological evolution of the active Yellow River (Huanghe) delta lobe (1976–2013): Dominant roles of riverine discharge and sediment grain size. *Geomorphology*, *292*, 115–127. https://doi.org/10.1016/j.geomorph.2017.04.042

Xu, H. (2006). Modification of normalised difference water index (NDWI) to enhance open water features in remotely sensed imagery. *International Journal of Remote Sensing*, *27*(14), 3025–3033. https://doi.org/10.1080/01431160600589179

Yamazaki, D., Trigg, M. A., & Ikeshima, D. (2015). Development of a global ~90m water body map using multi-temporal Landsat images. *Remote Sensing of Environment*, *171*, 337–351. https://doi.org/10.1016/j.rse.2015.10.014

Yamazaki, D., Ikeshima, D., Sosa, J., Bates, P. D., Allen, G. H., & Pavelsky, T. M. (2019). MERIT Hydro: A High-Resolution Global Hydrography Map Based on Latest Topography Dataset. *Water Resources Research*, *55*(6), 5053–5073. https://doi.org/10.1029/2019wr024873

Yan, D., Wang, K., Qin, T., Weng, B., Wang, H., Bi, W., et al. (2019). A data set of global river networks and corresponding water resources zones divisions. *Scientific Data*, *6*(1), 219. https://doi.org/10.1038/s41597-019-0243-y

Yang, X., Pavelsky, T. M., Allen, G. H., & Donchyts, G. (2020a). RivWidthCloud: An Automated Google Earth Engine Algorithm for River Width Extraction From Remotely Sensed Imagery. *IEEE Geoscience and Remote Sensing Letters*, *17*(2), 217–221. https://doi.org/10.1109/LGRS.2019.2920225

Yang, X., Qin, Q., Yésou, H., Ledauphin, T., Koehl, M., Grussenmeyer, P., & Zhu, Z. (2020b). Monthly estimation of the surface water extent in France at a 10-m resolution using Sentinel-2 data. *Remote Sensing of Environment,* *244*, 111803. https://www.sciencedirect.com/science/article/pii/S0034425720301735

Yin, S., Gao, G., Ran, L., Lu, X., & Fu, B. (2021). Spatiotemporal Variations of Sediment Discharge and In-Reach Sediment Budget in the Yellow River From the Headwater to the Delta. *Water Resources Research*, *57*(11), e2021WR030130. https://doi.org/10.1029/2021WR030130

Zhu, Q., Li, P., Li, Z., Pu, S., Wu, X., Bi, N., & Wang, H. (2021). Spatiotemporal Changes of Coastline over the Yellow River Delta in the Previous 40 Years with Optical and SAR Remote Sensing. *Remote Sensing*, *13*(10), 1940–1967. https://doi.org/10.3390/rs13101940

Zou, Z., Xiao, X., Dong, J., Qin, Y., Doughty, R. B., Menarguez, M. A., et al. (2018). Divergent trends of open-surface water body area in the contiguous United States from 1984 to 2016. *Proceedings of the National Academy of Sciences*, *115*(15), 3810–3815. https://doi.org/10.1073/pnas.1719275115